

JGR Atmospheres

RESEARCH ARTICLE

10.1029/2023JD038742

Key Points:

- Thompson scheme better reproduces raindrop median size and number concentration than two other schemes in a Guangzhou extreme rain event
- None of the three schemes examined adequately predicts the full variability of raindrop size distribution important for extreme rainfall
- Low raindrop concentration and excessively large sizes in simulations jointly cause the too weak collision-coalescence processes

Correspondence to:

M. Xue,
mxue@ou.edu

Citation:

Wang, H., Xue, M., Yin, J., & Deng, H. (2023). Comparison of simulated warm-rain microphysical processes in a record-breaking rainfall event using polarimetric radar observations. *Journal of Geophysical Research: Atmospheres*, 128, e2023JD038742. <https://doi.org/10.1029/2023JD038742>

Received 20 FEB 2023
Accepted 15 NOV 2023

Author Contributions:

Conceptualization: Hong Wang, Ming Xue, Jinfang Yin
Data curation: Jinfang Yin, Hua Deng
Methodology: Hong Wang, Ming Xue, Jinfang Yin
Resources: Jinfang Yin, Hua Deng
Software: Hua Deng
Supervision: Hong Wang, Ming Xue
Visualization: Hua Deng
Writing – original draft: Hong Wang, Jinfang Yin
Writing – review & editing: Hong Wang, Ming Xue, Jinfang Yin, Hua Deng

Comparison of Simulated Warm-Rain Microphysical Processes in a Record-Breaking Rainfall Event Using Polarimetric Radar Observations

Hong Wang^{1,2} , Ming Xue^{1,3} , Jinfang Yin⁴ , and Hua Deng²

¹Key Laboratory of Mesoscale Severe Weather, Ministry of Education and School of Atmospheric Sciences, Nanjing University, Nanjing, China, ²Guangzhou Institute of Tropical and Marine Meteorology/Guangdong Provincial Key Laboratory of Regional Numerical Weather Prediction, China Meteorological Administration, Guangzhou, China, ³Center for Analysis and Prediction of Storms and School of Meteorology, University of Oklahoma, Norman, OK, USA, ⁴State Key Laboratory of Severe Weather, Chinese Academy of Meteorological Sciences, Beijing, China

Abstract During 6–7 May 2017, a record-breaking nocturnal rainfall event occurred in Guangzhou, China, and it was a typical warm-sector heavy rainfall event under weak synoptic forcing. A prior observational study by the authors revealed that warm-rain microphysical processes were dominant and responsible for the record-breaking precipitation. In this study, the double-moment Morrison, Thompson and NSSL microphysics schemes in WRF are evaluated against polarimetric radar observations in their ability of reproducing observed microphysical characteristics. The Thompson scheme shows the greatest fidelity to the observed raindrop size distribution (RSD) median value, corresponding to the most amount of precipitation forecast. While the Morrison and NSSL simulations overestimate (underestimate) the raindrop size (number concentration), exhibiting continental-type convective precipitation. The three experiments slightly overestimate differential reflectivity (Z_{DR}), but significantly underestimate specific differential phase (K_{DP}) and liquid water content by about 30%–50%, implying the undervaluation of number of medium-sized raindrops. Examinations of the occurrence frequencies of Z_{DR} , K_{DP} , mass-weighted diameter, and logarithmic normalized intercept parameter for rain suggest that all three schemes fail to reproduce the full variability of observed RSD for the extreme rainfall. The vertical variations of RSD parameters and the Kumjian-Ryzhkov parameter space suggest that the collision-coalescence is the dominant warm-rain microphysical process but the simulated process is too weak. This may be attributed to the misrepresented RSD near the melting layer, where the raindrops with lower number concentration and larger sizes cannot grow through the collision-coalescence process as actively.

Plain Language Summary Extreme rainfall is of great concern due to its potential to cause major disasters. Cloud microphysics has been considered one of the main sources of uncertainty in predicting rainfall at cloud-resolving resolutions. This study investigates the performances of three commonly used schemes representing cloud precipitation processes in an extreme rainfall case that occurred in the warm and moist environment of South China. The Thompson scheme is found to perform better in simulating raindrop sizes and surface precipitation. None of the three schemes reproduces the full variation of observed raindrops, and all of them underestimate raindrop size growth through collision processes. These results suggest areas needing improvement in microphysics schemes for predicting extreme precipitation in sub-tropical regions.

1. Introduction

Heavy rainfall, one of the most devastating natural hazards over South China, frequently occurs during the pre-summer (April to mid-June) rainy season (Luo et al., 2017). Based on the strength of synoptic forcing (Huang et al., 1986), heavy rainfall events are usually categorized into two major types, frontal heavy rainfall and warm-sector heavy rainfall (WR). The frontal heavy rainfall is closely linked to dynamic lifting by fronts or shear lines, whereas WR is within weakly forced synoptic environment often with a smaller horizontal scale. At present, both global and regional numerical weather prediction (NWP) models have poor skill in forecasting heavy rainfall over South China, especially for WR (Huang & Luo, 2017). Studies (Huang et al., 2020; Luo et al., 2020) have demonstrated that microphysical processes are important to accurately predicting heavy rainfall over South China, but the relative contributions of warm-rain, riming, and ice-phase processes remain unclear.

Meteorologists often use NWP models with sophisticated physics parameterization schemes to simulate and understand the mechanisms of weather systems (Gao et al., 2021; Tao et al., 2003). As model resolution increases, the microphysics schemes become increasingly important for precipitation forecasting in NWP models, with bulk microphysics schemes most used (Mansell et al., 2010; Morrison et al., 2009). In recent decades, bulk microphysics schemes have become more complex and are including more hydrometeor species and more processes. However, the complexity of microphysics scheme does not necessarily lead to good forecast. Therefore, objective assessments of microphysics schemes are essential for improving quantitative precipitation forecast skill of NWP models, and their performances are dependent on weather regimes and types of precipitation. Due to the lack of observations, earlier evaluation studies have mostly focused on the comparison of precipitation, latent heating, and moisture budget using limited in-situ observations and small amount of remote sensing observations collected during field campaigns (Lou et al., 2003; Tao et al., 2003).

In recent decades, the observational technologies have seen great progress, especially with polarimetric weather radars that have become widely used in researches and operations (Kumjian, 2013; Zhang et al., 2019; Zhao et al., 2019). Many interesting features of severe storms, such as the differential reflectivity (Z_{DR}) and specific differential phase (K_{DP}) columns, and Z_{DR} arc, have been found (Kumjian & Ryzhkov, 2008; Liu et al., 2018; Wang et al., 2019). Meanwhile, these measurements also provide additional information for evaluating microphysics schemes. For instance, Z_{DR} , defined as the logarithmic ratio of the reflectivity factors at horizontal and vertical polarizations, is particularly useful for determining the size of raindrops, while K_{DP} can be used to infer liquid water content (LWC). The combination of reflectivity factor for horizontal polarizations (Z_H) and Z_{DR} can reveal characteristics of the raindrop size distribution (RSD), as well as “fingerprints” of microphysical processes, such as evaporation, coalescence, and breakup (Carr et al., 2017; Kumjian, 2013).

Benefiting from their microphysical information content, high spatial resolution and coverage, polarimetric radar observations have been used to evaluate microphysics schemes in various severe storm simulations. For example, Brown et al. (2016) evaluated six microphysics schemes in the Weather Research and Forecasting model (WRF) for hurricanes Arthur and Ana. They found that most of the schemes produced a higher frequency of larger raindrops than observed. Wang et al. (2020) and Wu et al. (2021) assessed the model performance in simulating typhoons Matmo (2014) and Nida (2016), and highlighted the importance of reproducing warm-rain (ice-phase) processes for the heavy precipitation in the inner (outer) rainbands of the typhoon, respectively. Studies on supercells (Johnson et al., 2016; Putnam et al., 2014), hurricanes (Yang et al., 2019), and mesoscale convective systems (Putnam, Xue, Jung, Snook, & Zhang, 2017) indicated that double-moment schemes can better reproduce well-known polarimetric radar signatures than single-moment schemes, although in simulations for a squall line in Taiwan a single-moment scheme performed better based on the contour frequency by altitude diagrams for polarimetric parameters (You et al., 2020). All in all, microphysics schemes have considerably different performance in simulating different types of storms over different climate regions. The applicability and performance of different microphysics schemes in a given climate region, such as South China, still need more research.

Furthermore, studies (Huang et al., 2020; Luo et al., 2020; Xu et al., 2018) show that WR in South China tends to have low-centroid cumulonimbus structures associated with weak updrafts, and high precipitation efficiency due to abundant water vapor. These characteristics imply that warm-rain processes are very active in WR events (Lu et al., 2023), but the relative importance of different warm-rain processes (i.e., evaporation, coalescence, size sorting, and breakup) and the ability of different microphysics schemes in simulating these processes deserve further investigation.

During 6–7 May 2017, a record-breaking nocturnal rainfall event occurred in Guangzhou, which is a typical WR under weak synoptic forcing (Wang et al., 2023). This study will compare the simulated microphysics characteristics with three two-moment microphysics schemes within WRF for this extreme rainfall case using the Guangzhou S-band polarimetric radar (marked as GZPR in Figure 1b) observations. Several questions will be addressed: (a) Are the polarimetric variables and RSD simulated by different microphysics schemes consistent with observations? (b) How do the vertical variations of RSD parameters impact the surface precipitation? (c) What is the dominant warm-rain process responsible for these differences? How active are these processes?

The remainder of the paper is organized as follows: Section 2 describes the observations, data analysis methodologies, and numerical experiment configurations. Section 3 presents the evaluations of simulated precipitation, polarimetric variables, and RSD. Section 4 examines the warm-rain microphysical processes differences among

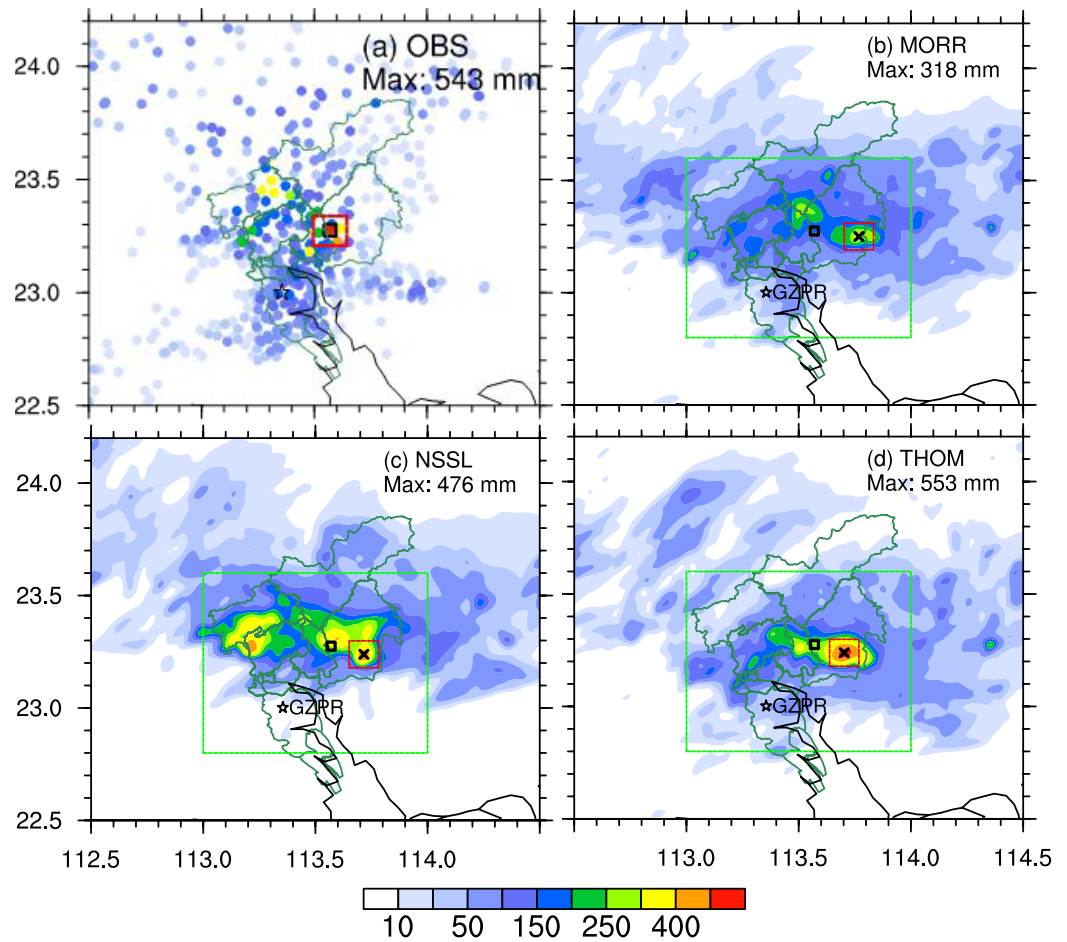


Figure 1. The (a) observed and (b)–(d) simulated total precipitation from 1600 UTC 6 May to 0700 UTC 7 May. The black box represents the location of maximum observed total precipitation and the black star marks the location of GZPR. The green lines mark the borders of the districts of Guangzhou. The maximum total precipitation is provided in the top-right-hand corner of the panel and its location is marked by the black cross. The red boxes are centered on the respective maximum accumulate precipitation and are used for diagnostic analyses focusing on the maximum precipitation centers. The green boxes are used for calculation of moisture flux. The horizontal and vertical axis labels are in longitude and latitude degrees.

the schemes and investigates the key factor producing the unique RSD characteristics. A summary and conclusions are presented in the final section.

2. Data and Methodology

2.1. The “5.7” Guangzhou Extreme Rain Event

A local extreme rain event occurred in Guangzhou during 6–7 May 2017, with record-breaking 3-hr accumulated precipitation amounts of 382 mm during the 2100 UTC 6 May - 0000 UTC 7 May period, which became the new records for Guangdong Province. The 15-hr accumulated rainfall exceeded 100 mm at 128 rain gauges, or at 30% of automatic weather stations (AWS) in Guangzhou (Figure 1a). The event brought many disasters, including urban waterlogging, landslides, and mudslides, to Guangzhou. However, this case occurred on the edge of the subtropical high without any obvious synoptic-scale weather systems (e.g., front, low-level jets). Namely, it is an extreme rainfall case under weak synoptic-scale forcing in the pre-summer rain season over South China (Xu et al., 2018). Both operational NWP models (e.g., those of European Center for Medium-Range Weather Forecasts, Global/Regional Assimilation and Prediction System Mesoscale Model of the Chinese Meteorological Administration) and forecasters significantly underestimated the precipitation intensity of this event (Wu et al., 2018).

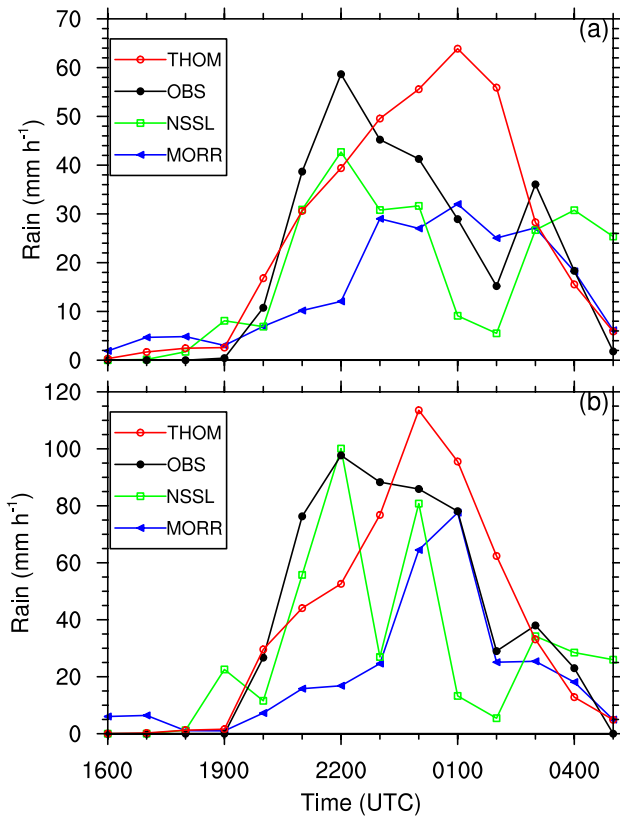


Figure 2. Time series of (a) average hourly rainfall over the red boxes in Figure 1, and (b) the hourly rainfall at the point of maximum accumulated precipitation (the black box in Figure 1a and black x in Figures 1b–1d) from 1600 UTC 6 May to 0500 UTC 7 May 2017.

of cloud droplets, but the MORR and THOM schemes prescribe the cloud droplet total number concentrations as constant values. In this paper, the default values of 2.5×10^8 and 10^8 m^{-3} are used for MORR and THOM, respectively. The initiation of cloud droplets in the NSSL scheme follows Ziegler (1985). The number concentration initiated at cloud base is adapted from Twomey (1959) with default prescribed values of cloud condensation nuclei (CCN) concentration of $6 \times 10^8 \text{ m}^{-3}$. Although the three microphysics schemes contain most of the cloud microphysical processes discussed in Braham and Squires (1974), there are significant differences among them. Taking auto-conversion as an example, the MORR scheme uses the equation of Khairoutdinov and Kogan (2000).

One of its advantages is that there is no need to define a threshold. The NSSL and THOM schemes adopt the approach of Berry and Reinhardt (1974), in which not only cloud water content but also cloud number concentration is incorporated. The auto-conversion rates from different schemes can differ by several orders of magnitude (Xu et al., 2020). All in all, many microphysical processes deserve in-depth evaluations, but most of them do not have corresponding observations. Therefore, this study would focus on the microphysical processes (e.g., collision–coalescence) on which information can be retrieved from polarimetric radar measurements.

2.3. Polarimetric Radar Measurements

During the rainfall event, radar echoes mainly occurred near GZPR radar station (Figure 1 black star), within a 100 km range. Thirteen hours (i.e., 1600 UTC 6 May to 0500 UTC 7 May) of GZPR Level II data were obtained

Table 1
Prognostic Variables in the Microphysics Schemes Evaluated in This Study

| | MORR | NSSL | THOM |
|----------------|----------|----------|----------|
| Cloud droplets | Q | q, N_i | q |
| Rain | q, N_i | q, N_i | q, N_i |
| Cloud ice | q, N_i | q, N_i | q, N_i |
| Snow | q, N_i | q, N_i | q |
| Graupel | q, N_i | q, N_i | q |
| Hail | NA | q, N_i | NA |

Note. Here q denotes mass mixing ratio, N_i denotes total number concentration. Schemes that do not contain a given hydrometeor category are listed as not applicable (NA).

2.2. Experiment Design and Microphysics Schemes

The Guangzhou extreme rain case is simulated using three different microphysics schemes in the WRF-ARW (v3.9.1). Details about the WRF configurations used in this study can be found in Section 3 of Yin et al. (2020). The simulations are configured with three two-way nested domains at 12, 4, and 1.33 km horizontal grid spacings (please refer to Figure 2 of Yin et al. (2020) for the domain sizes). All domains use 57 vertical levels with stretching below 850 hPa and above 200 hPa. All simulations use the following physics parameterizations: the rapid radiative transfer model (Mlawer et al., 1997) for both shortwave and longwave; the Yonsei University PBL scheme (Hong et al., 2006); the MM5 Monin–Obukhov similarity scheme (Zhang & Anthes, 1982); the Noah-MP land surface scheme (Niu et al., 2011); the cumulus parameterization scheme (Kain, 2004) in the two outer coarse-resolution domains, but not in the 1.33 km domain.

The model is initialized with the NCEP GFS Final Analysis (FNL) 0.25° data at 1200 UTC 6 May and is integrated for 20 hr. The 6-min intervals of model output match the intervals of GZPR observations. Observational studies (Wang et al., 2023; Xu et al., 2018) show that urban heat island is critical for convective initiation of this case. To realistically simulate the urban heat island effects, the experiments apply observation nudging toward hourly surface AWS observations from 1200 UTC 6 May to 0000 UTC 7 May 2017, using the four-dimensional data assimilation function of WRF (Seaman et al., 1995).

The three microphysics schemes evaluated are the Morrison scheme (MORR, Morrison et al. (2009)), the National Severe Storms Laboratory scheme (NSSL, Mansell et al. (2010)), and the Thompson scheme (THOM, Thompson et al. (2008)). Table 1 lists the hydrometeor categories and variables predicted in each scheme. Specifically, the NSSL is fully double moment, the MORR and THOM are only partially double moment. MORR is double moment in rain, ice, snow, and graupel. The THOM scheme is double moment in cloud ice and rain (Table 1). The NSSL scheme predicts the number concentration

for our evaluation. GZPR was upgraded to polarimetric radar from the China New Generation Weather Radar/SA (CINRAD/SA) in March 2016. GZPR transmits and receives the horizontal/vertical polarimetric pulses, the same as the polarimetric WSR-88D radars of the U.S. National Weather Service. Strict quality control to remove non-meteorological and unphysical radar echoes was performed as described in Wang et al. (2018). The data were then gridded to the model resolution using 88D2ARPS software from the Center for Analysis and Prediction of Storms.

2.4. Microphysical Parameter Retrieval

To obtain RSD-related parameters, The RSD retrieval algorithm from Wang et al. (2019) is adopted for GZPR observations. The LWC, mass-weighted mean diameter (D_{mr}) and normalized intercept (N_{wr}) for raindrop are estimated from the combination of Z_H and Z_{DR} :

$$LWC = 1.023 \times 10^{-3} Z \times 10^{(-0.0742Z_{DR}^3 + 0.511Z_{DR}^2 - 1.511Z_{DR})}, \quad (1)$$

$$D_{mr} = 0.7218 \times Z_{DR} + 0.955, \quad (2)$$

$$N_{wr} = \frac{4^4}{\pi \rho_w} \left(\frac{LWC}{D_{mr}^4} \right). \quad (3)$$

The coefficients are fitted from raindrop disdrometer observations, which is inaccurate for ice or mixed phase particles, so Equations 1–3 only apply to pure rain. The measurement errors for Z_H and Z_{DR} for well calibrated S-band radars are typically 1 dBZ and 0.2 dB, respectively. The power-law statistical uncertainties of D_{mr} and LWC are about 0.15 mm and 0.8 g m⁻³, respectively.

The method from Ryzhkov et al. (2018) is adopted to estimate ice water content (IWC). In this method, the IWC is retrieved from K_{DP} and Z_{dr} according to

$$IWC = 4.0 \times 10^{-3} \frac{K_{DP} \lambda}{1 - Z_{dr}^{-1}}, \quad (4)$$

where Z_{dr} is in linear units ($Z_{dr} = 10^{Z_{DR}/10}$) and λ is the radar wavelength in mm. To avoid the interference from liquid and mixed phase particles, this method is valid above the melting layer. Compared with snow disdrometer measurements, this method underestimates the IWC (Ryzhkov et al., 2018). The comparison results also show that the method is not sensitive to the shape of ice particles, but is affected by the degree of riming. It has a better chance to work at lower temperatures (i.e., -10 to -20°C) with lower likelihood of riming. Additionally, large Z_{DR} errors will reduce the accuracy of the method if the Z_{DR} is low. To avoid this situation, the approach of Wu et al. (2021), where a Z_{DR} floor of 0.3 dB is set if $Z_{DR} < 0.3$ dB, is adopted. It should be noted that the errors of polarimetric radar measurements would be larger above the melting layer (i.e., 0.3° km⁻¹ for K_{DP}), resulting in more uncertainty for the retrieved IWC, so the IWC result would only be used for qualitative analysis.

2.5. Polarimetric Radar Simulator

The polarimetric radar simulator developed by Wang et al. (2016) is used to calculate polarimetric variables from the output of microphysics schemes (i.e., mixing ratios and number concentrations). Because the backscattering of cloud water and cloud ice is minimal, only rain, snow, graupel, and hail categories are considered. The Rayleigh-Gans scattering theory is adopted to calculate the complex scattering amplitudes. Moreover, the simulator uses the ratio of ice and water masses to characterize the melting model of snow, graupel, and hail, following Jung et al. (2008), and utilizes Fisher distribution to describe the canting angle distributions of particles.

3. Results

3.1. Rainfall Prediction With Different Microphysics Schemes

The accumulated rainfall from the WRF simulations using three microphysics schemes are compared with rain gauge observations near Guangzhou (Figure 1). The observed heavy rainfall (Figure 1a) is predominantly concentrated over the center of Guangzhou, with a maximum accumulation of 543 mm from 1600 UTC 6 May to 0700 UTC 7 May (at the black box in Figure 1a). In general, the three experiments place the simulated precipitation in Guangzhou, but there are differences in the spatial distribution and intensity of rainfall across the schemes.

Experiment MORR (Figure 1b) produces the smallest amount of 15-hr accumulated rainfall (318 mm) whereas experiment THOM (Figure 1d) simulates a maximum accumulation of 553 mm, close to the observed 543 mm. The simulated rain of experiment NSSL basically falls on two regions, somewhat like observations, but it overestimates the area of 250 mm rainfall. The three experiments produce similar locations of maximum accumulated precipitation (black crosses in Figure 1), which are about 25 km east of observed maximum. For exploring the evolution of extreme rainfall and its microphysical processes, we define a squared area with a width of 11 model grid intervals (about 14.6 km, red dotted box in Figure 1) centered at the respective maximum of accumulated precipitation (black box and black cross in Figure 1).

Figure 2a compares the time series of hourly rainfall rates between observations and simulations averaged over the red boxes in Figure 1, which are centered on the respective maximum total rainfall locations. The observed average rainfall starts at 1900 UTC 6 May, and has a maximum of 59 mm hr⁻¹ at 2200 UTC 6 May, and a secondary maximum of 36 mm hr⁻¹ at 0300 UTC 7 May. All three experiments simulate the start and end times of rainfall reasonably well. The maximum of the THOM experiment (63 mm hr⁻¹) is the closest to the observed maximum, although there is a time lag of 3 hr. The NSSL experiment reproduces the observed bimodal distribution with two peaks, but underestimates the precipitation intensity with a maximum of about 43 mm hr⁻¹ that occurs at the correct time. Its secondary maximum is very close to the observed value and differs in timing by only 1 hr. The MORR experiment significantly under-predicts the peak precipitation rate, reaching only 33 mm hr⁻¹ (Figure 2a).

In terms of the hourly rainfall at the point of maximum accumulated precipitation (Figure 2b), The NSSL scheme (green line in Figure 2b) produces a peak hourly rainfall rate that matches the observed very closely in both timing and amount, but its rainfall rate fluctuates significantly over the next few hours, unlike observation. The hourly rainfall pattern of the THOM experiment is more consistent with the observations, showing a single dominant maximum of ~115 mm hr⁻¹ that is over 15 mm hr⁻¹ too large and delayed by 2 hr. As with the area average rainfall, the MORR experiment also underestimates the maximum by about 20 mm hr⁻¹ and its peak is 3 hr late (blue line in Figure 2b). The NSSL experiment produces the best time evolution of the precipitation rate with two peaks while the THOM experiment better captures the maximum rainfall rate. In this study, we focus mainly on the microphysical characteristics of extreme rainfall within 2 hr near the maximum hourly precipitation, which will be quantitatively analyzed in the following section.

Cloud droplet is an important part of precipitation formation. Xiao et al. (2023) carried out an ensemble of sensitivity experiments in which the initial cloud droplet number concentration was set to two values representing clean and polluted environments. They found that the changes in total surface precipitation of a simulated south China squall line ranged from -14% to 4%. Kedia et al. (2019) assessed the impact of aerosols on two heavy rainfall events in India using coupled meteorology-chemistry-aerosol (WRF-Chem) model simulations. They found an overall enhancement of total cumulative rainfall as high as 20% due to aerosols and gas chemistry in certain regions of their simulation domain. While the aerosol effects on precipitation is not the focus of this study, we did run an additional sensitivity experiment in which the prescribed cloud droplet total number concentration in the THOM scheme is set to $2.5 \times 10^8 \text{ m}^{-3}$ instead of the default value of 10^8 m^{-3} . These values are more representative of continental and marine environments, respectively. Since Guangzhou is a coastal city with most low-level inflow coming from the ocean, it is unclear which value is more representative of the environment of the precipitation system in this study. The sensitivity experiment with the higher cloud droplet number concentration produces a better hourly rainfall time series, placing the hourly precipitation peak correctly at 2200 UTC (cf., Figure 2), but a lower average peak hourly intensity (~40 mm hr⁻¹ instead of the original ~65 mm hr⁻¹, compared to the observed peak of ~60 mm hr⁻¹, not shown) than the original THOM experiment. We plan to perform a systematic study on the aerosol effects on the extreme precipitation of this case separately.

3.2. Prediction of Moisture Convergence and Convective Updraft

Moisture and upward motion are two essential ingredients for heavy rainfall. Therefore, moisture flux and average vertical velocity are used to examine the moisture supply and updraft for heavy rainfall, respectively. The moisture fluxes are calculated following the algorithm documented in Huang et al. (2019). The moisture flux into the main heavy rainfall area (green boxes in Figures 1b–1d, 113–114°E, 22.8–23.6°N) is calculated using the following equation:

$$QFlux_i = \int_0^{L_W} Q_v U_W dl_s + \int_0^{L_E} Q_v U_E dl_s + \int_0^{L_S} Q_v V_S dl_s + \int_0^{L_N} Q_v V_N dl_s, \quad (5)$$

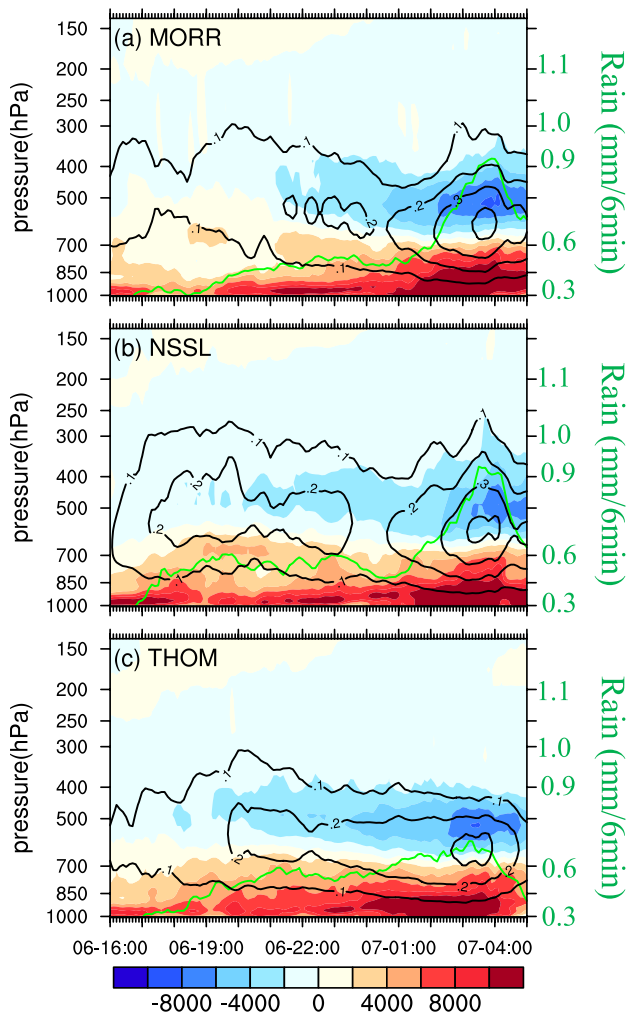


Figure 3. Time-height cross sections of total vertical moisture flux (shaded, $\text{kg kg}^{-1} \text{m}^2 \text{s}^{-1}$) and average vertical velocity (black contours, m s^{-1}) from 1600 UTC 6 to 0500 UTC 7 May 2017 within the green boxes in Figures 1b–1d. The green solid curves are average precipitation rates (mm (6 min)^{-1}) within the area ($22.8\text{--}23.6^\circ\text{N}$, $113\text{--}114^\circ\text{E}$) from the total moisture flux.

where Q_{Flux} is the total moisture flux at a given level, through the four boundaries into the heavy rainfall area. Q_v , U , V , and L are water vapor mixing ratio, east-west wind, north-south wind, and the length of each boundary, respectively. Subscripts W, E, S, and N represent west, east, north, and south, respectively. For the wind vector component normal to boundary, inward direction is positive, and outward direction is negative. The average vertical motion at different levels and average precipitation are also calculated in the same area as the moisture flux.

Figure 3 shows the time-height cross sections of total moisture fluxes, average vertical motion, and average precipitation rates over the budget box. The three experiments produce a similar time-height pattern of moisture fluxes. There are strong inward moisture fluxes in the lower troposphere, mainly below 600 hPa, with maxima of over $10,000 \text{ kg kg}^{-1} \text{m}^2 \text{s}^{-1}$ that happen near the time of maximum rainfall. Above ~ 600 hPa, the net moisture flux is outward while the maximum upward motion occurs at the same dividing level of 600 hPa. In the MORR and NSSL experiments, the 0.1 m s^{-1} contour of average upward motion reach between 400 hPa and 300 hPa levels with the maximum of $>0.4 \text{ m s}^{-1}$ at 0330 UTC 7 May, consistent with the timing of maximum moisture flux ($\sim 10,000 \text{ kg kg}^{-1} \text{m}^2 \text{s}^{-1}$) and maximum average precipitation rate ($>0.9 \text{ mm 6 min}^{-1}$). The updraft distribution of THOM experiment differs from those of MORR and NSSL experiments, with the 0.1 mm hr^{-1} contour mostly reaching only ~ 400 hPa and the maximum amount is also lower at $\sim 0.3 \text{ m s}^{-1}$. Correspondingly, the average precipitation rate reaches only $\sim 0.7 \text{ mm 6 min}^{-1}$.

3.3. Polarimetric Structure for the Model and Observations

During the analysis period, the observed storms go through the convection initialization, development, maturity, and dissipation stages. At 2154 UTC 6 May, the observed storms reach the maturity stage with a maximum observed Z_{DR} of 4.6 dB and a maximum K_{DP} of $5.2^\circ \text{ km}^{-1}$ at the 1.5 km height (Figures 4a2–4a3). All simulations capture the general distribution with the main radar echoes located north of GZPR (Figures 4b1–4d1). Also, all experiments simulate the size and strength of convective regions (black contours in Figure 4) that are generally comparable to observations although the detailed structures have noticeable differences from observations. Following Wang et al. (2019), the convective regions are identified based on the depth of radar reflectivity. In contrast to Z_H , the simulations produce quite different Z_{DR} and K_{DP} values among different microphysics schemes. All experiments underestimate the maximum Z_{DR} values compared to observations (Figures 4b2, 4c2, and 4d2). The simulated K_{DP} varies more than Z_{DR} across the experiments. It should be noted that Figure 4 only compares the polarimetric structures at a given time, and of course it does not represent all differences in microphysical characteristics.

For forecast verification, it is common to compare observations and model simulation valid at the same time. However, the position error that grows fast during the forward model integration makes it difficult to compare storms at the same locations. Therefore, in addition to the horizontal distribution of polarimetric variables (Figure 4), we will further examine the frequency statistics of polarimetric variables. The statistical database encompasses the observed and simulated polarimetric variables over 121 model grid points centered on the respective maximum accumulated precipitation grid (the red boxes in Figure 1). To evaluate the performance of different microphysics schemes in the extreme rainfall simulation, the time windows of the data samples are 2 hr centered on the respective maximum hourly rainfall (i.e., observations at 2100–2300 UTC 6 May; MORR at 0000–0200 UTC 7 May; NSSL at 2100–2300 UTC 6 May; THOM at 2300 UTC 6 May–0100 UTC 7 May).

The joint probability density function (JPDF) is created in ZH-ZDR space and ZH-KDP space, according to Brown et al. (2016). These JPDFs are normalized by the maximum frequency, such that 100% means the most

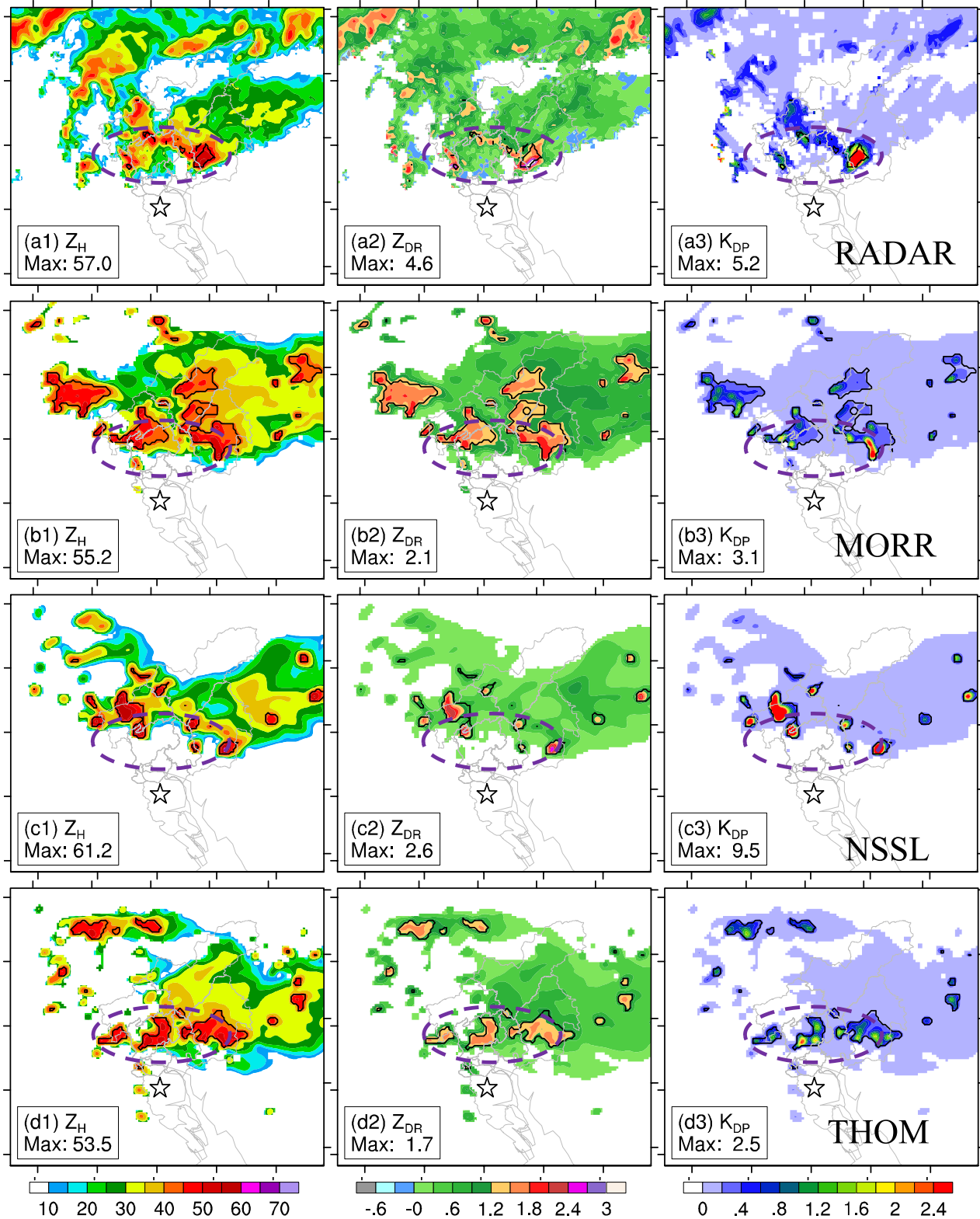


Figure 4. CAPPI of the (a1–d1) Z_H (units: dBZ), (a2–d2) Z_{DR} (units: dB), and (a3–d3) K_{DP} (units: $^{\circ} \text{ km}^{-1}$) at 1.5 km height from the observations (a1–a3), and simulations using Morrison scheme (b1–b3), NSSL scheme (c1–c3), and Thompson scheme (d1–d3) at 2154 UTC 6 May 2017. The star represents the location of GZPR radar. The black contours indicate the convective regions.

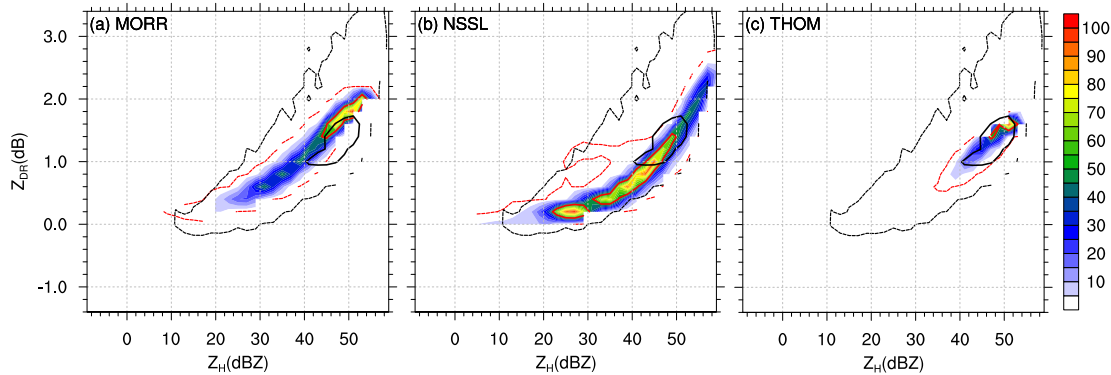


Figure 5. Frequency of occurrences (color shaded) of ZH (dBZ) and ZDR (dB) normalized by the maximum frequency of simulation from (a) MORR, (b) NSSL, (c) THOM. The red contours indicate the simulated percentages at 1% (dashed) and 50% (solid), while the corresponding observations from GZPR are given in black contours.

commonly occurring joint value of ZH and ZDR (*KDP*), and the values over 50% are referred to as the modal distribution following Henc and Houze (2011). The JPDF of the observed ZH and ZDR below 4 km height is characterized by peak frequencies at 49 dBZ and 1.4 dB (black contours in Figure 5). The modal distribution is contained within 41–52 dBZ in ZH and 0.9–1.7 dB in ZDR. There are 7.2% of samples exceeding 50 dBZ of ZH and 2 dB of ZDR.

In contrast, the MORR experiment has modal distributions that extend from 44 to 53 dBZ in ZH and from 1.4 to 2.1 dB in ZDR (Figure 5a). The ZDR values in the MORR experiment are larger than those in observations, implying that the MORR simulation produces larger raindrop sizes than the observations, especially for ZH over 40 dBZ. In the NSSL experiment, more than 50% of the sample points exhibit JPDF of ZH -ZDR in the range of 22–50 dBZ and 0.1–1.4 dB (Figure 5b). Among the simulations, THOM shows the greatest fidelity to the radar observations (Figure 5c). Peak frequencies from the THOM simulation are closest to the observations, followed by the MORR, and NSSL experiment performs the worst. Another noticeable feature is that the MORR experiment has more large raindrops (i.e., 10%) with ZH exceeding 50 dBZ and ZDR exceeding 2 dB than observations (7.2%). The NSSL experiment is second (i.e., 8.2%) while there are almost no large raindrops (~0.0%) in the THOM experiment. The ZH -ZDR distribution range for the THOM experiment is very narrow, only equivalent to 20% of the observations. The narrowest distribution range should be closely related to the upper limit of raindrop diameter in the THOM scheme.

Figure 6 shows the JPDF of ZH and *KDP*. Because the intrinsic values of *KDP* are very small for stratus clouds, especially for light rain, meaning these data contain a lot of noise (Kumjian, 2013). Therefore, we only use the data from convective regions to calculate the JPDF of ZH and *KDP*. In the convective regions, all simulations, and

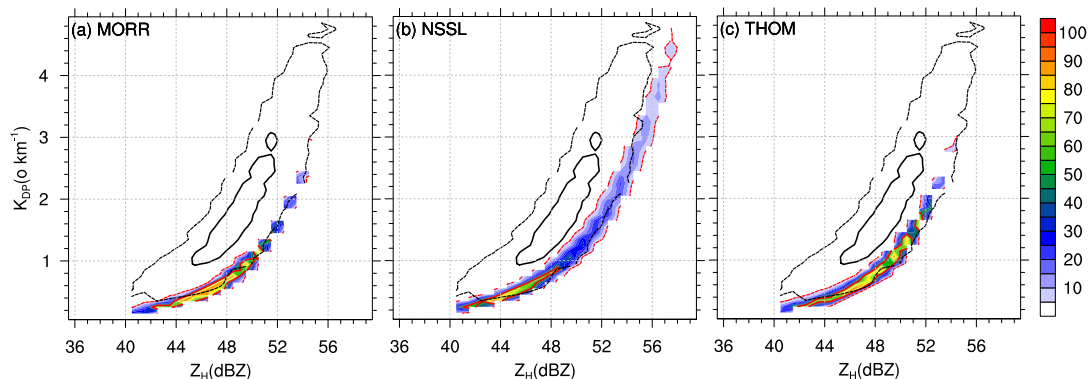


Figure 6. Frequency of occurrences (color shaded) of ZH (dBZ) and *KDP* ($^{\circ} \text{km}^{-1}$) in convective area normalized by the maximum frequency of simulation from (a) MORR, (b) NSSL, and (c) THOM. The red contours indicate the simulated percentages at 5% (dashed) and 50% (solid), while the corresponding observations from GZPR are given in black contours.

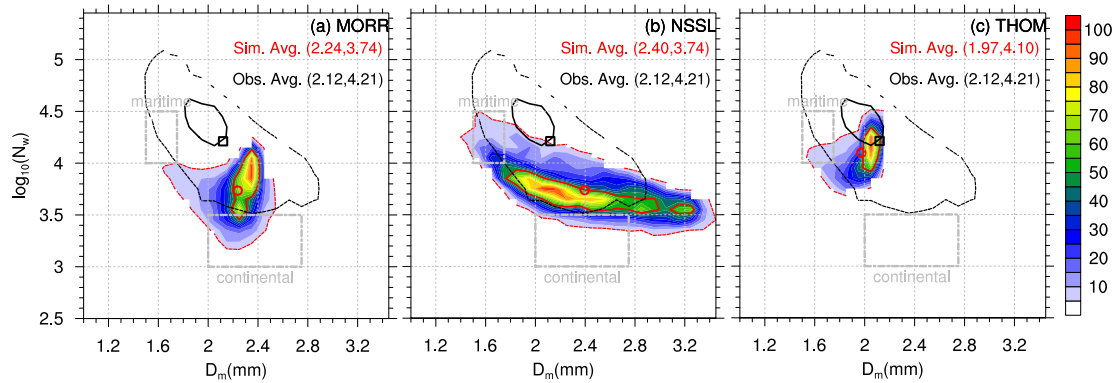


Figure 7. Frequency of occurrences (color shaded) of D_{mr} (mm) and logarithmic N_{wr} ($\text{mm}^{-1} \text{m}^{-3}$) of simulated RSD for the convective precipitation from (a) MORR, (b) NSSL, and (c) THOM experiments over the convective regions. The observed and simulated percentages at 50% (5%) are black and red solid (dashed) line, respectively. The observed and simulated averages are mark with a black box and red circle, respectively. The two rectangles represent the maritime and continental types of convective precipitation reported by (Bringi et al., 2003).

the observations exhibit a large slope between ZH and KDP, suggesting a rapid increase of KDP with the increase of ZH. The modal distributions of three simulations are located at the lower left of observed modal distributions. This indicates that all three experiments underestimate KDP. Meanwhile, the three experiments exhibit lower frequencies (9.8%, 18.1%, and 9.8% for MORR, NSSL, and THOM experiments, respectively) for ZH exceeding 50 dBZ and KDP exceeding 2.0°km^{-1} than observations (i.e., 35.3%), again showing undervaluation of KDP. In all experiments, the simulation error of KDP is significantly greater than that of ZDR. Lastly, the three simulations exhibit narrower spread in ZH -ZDR space and ZH -KDP space (dashed contours in Figures 5 and 6). It confirms that these double-moment microphysics schemes have realized variations in the intercept and slope parameters in the RSD model, but they are still unable to represent the full variability of observed RSD. Previous studies (Putnam, Xue, Jung, Snook, & Zhang, 2017; Wang et al., 2020; Wu et al., 2021; Yang et al., 2019) have also shown that neither single- nor double-moment schemes can faithfully reproduce the full variability of observed RSD. The narrower spread is directly related to the nature of double-moment schemes in which all radar variables are uniquely related to mixing ratios and number concentrations. Namely, only the intercept and slope parameters are variable in the RSD model.

To further evaluate the simulated RSD, a JPDF of particle size (D_{mr}) and number concentration (N_{wr}) for the raindrops of convective precipitation is calculated and normalized by the maximum occurrence frequency for observations and simulations (Figure 7). The measurements from GZPR shows that most raindrops (frequency 50%) are distributed in the range of 1.8–2.1 mm for D_{mr} and 4.2–4.6 for $\log_{10} N_{wr}$ with mean values of 2.12 mm and 4.21, respectively. In other words, the number concentration is representative of maritime convective precipitation (Bringi et al., 2003) while the particle size is close to that of continental clusters, that is, the raindrops are both relatively large in size and many in number. The accumulated precipitation can reach 543 mm because there are abundant medium-sized raindrops with diameters of 1–2 mm.

The MORR experiment produces the largest deviation with greater D_{mr} (mean value 2.24 mm) and lower $\log_{10} N_{wr}$ (mean value 3.74) than the observations (Figure 7a). In particular, the MORR scheme seriously underestimates the number concentration of raindrops with sizes between 1.5 and 2.0 mm. This is consistent with its worst precipitation forecast. The NSSL experiment reproduces the shape of observed RSD (Figure 7b), but underestimates $\log_{10} N_{wr}$ and produces too much raindrops with sizes exceeding 2.9 mm. The latter leads to the largest mean D_{mr} of 2.4 mm among the three experiments. Like the JPDF of polarimetric variables, the THOM experiment shows the smallest variability of D_{mr} - N_{wr} , but the mean value shows the greatest fidelity to the observations (Figure 7c). It produces the most abundant medium-sized raindrops among the three schemes, consistent with its most amount of precipitation produced. However, its D_{mr} is cut off at 2.12 mm because the scheme limits the maximum raindrop size to 5 mm. This also leads to no raindrops with ZH exceeding 50 dBZ and ZDR exceeding 2 dB in the THOM experiment (Figure 5c). The difference of simulated RSD can be partly attributed to the different treatments of cloud droplet concentration among the three microphysics schemes. It should be noted again that the default THOM experiment prescribes cloud droplet total number concentration value of 10^8m^{-3} ,

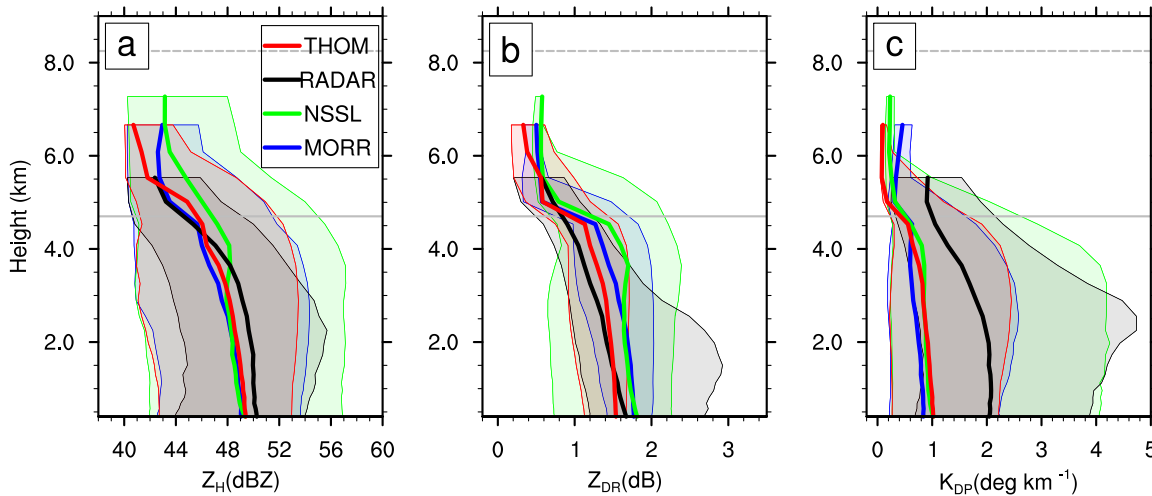


Figure 8. Composite vertical profiles of median (a) Z_H , (b) Z_{DR} , and (c) K_{DP} of the convective precipitation obtained from GZPR and WRF simulations using Morrison, NSSL, and Thompson microphysics schemes. The shaded polygons are the range between 5th and 95th quantiles. The profiles are not shown when the sample size is less than 200 in each layer. The gray lines indicate the level of 0°C and -20°C , respectively.

which is considered more representative of marine clouds. Generally, the three experiments do not reproduce the full variability of observed $D_{mr} - N_{wr}$.

3.4. Vertical Distributions of Polarimetric Radar Fields and Hydrometeors

The vertical structure of convective storms is to a significant extent influenced by treatment of microphysical processes (Liu et al., 2018; Wu et al., 2021). To examine the differences, the vertical profiles of polarimetric variables and microphysical parameters are compared.

Figure 8 shows the vertical distribution of polarimetric radar variables of the three simulations and the GZPR observations. Below the melting layer, the three schemes show comparable Z_H in the terms of median and range between 5th and 95th quantiles, with a small median deviation of -1.5 dBZ from the observations (Figure 8a). The three schemes have larger median Z_{DR} values indicating large rain drops, especially in the MORR and NSSL experiments whose deviations are about 0.3 dB. These discrepancies between simulated and observed Z_{DR} from this study are similar to those described in Yang et al. (2019) for the extreme rainfall from Hurricane Harvey (2017). The observed Z_{DR} increases from the melting layer to the ground by about 0.8 dB, which indicates

marked growth of raindrops through collision-coalescence processes (Carr et al., 2017). The simulations do not reproduce this structure well, however, with most of the Z_{DR} increase occurring near the melting level instead of throughout the lower levels (Figure 8b). In addition, the three experiments have a large bias in the Z_{DR} range below 3 km altitude, especially underestimating the 95th quantile. All three simulations seriously underestimate median K_{DP} at all altitudes, whose deviation exceeds 50% below 2.5 km (Figure 8c). The shortage of raindrop number, especially the medium-sized raindrops (Figure 7), means low LWC, resulting in small K_{DP} in the simulations. The underestimation of K_{DP} also appears in the simulations of a mesoscale convective system in the United States (Putnam, Xue, Jung, Zhang, & Kong, 2017; You et al., 2020). In the term of K_{DP} range, the NSSL scheme has better skill than the MORR and THOM schemes.

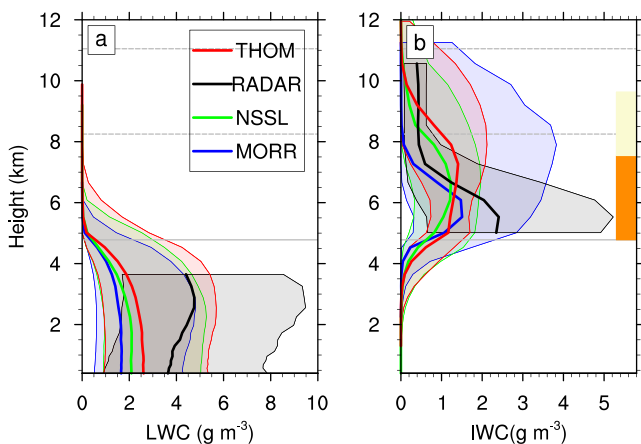


Figure 9. As in Figure 8, but for (a) liquid water content, and (b) ice water content. The yellow and orange shadings denote the “aggregation zone” and “riming zone”, respectively.

The IWC and LWC in each simulation are calculated to compare with the estimation from the GZPR observations (Figure 9). Since the LWC retrieval algorithm is inaccurate for ice- and mixed-phase particles, only the LWC below the melting layer is shown in Figure 9a. Similar to the median K_{DP} (Figure 8c), all simulations underestimate the median LWC at each level

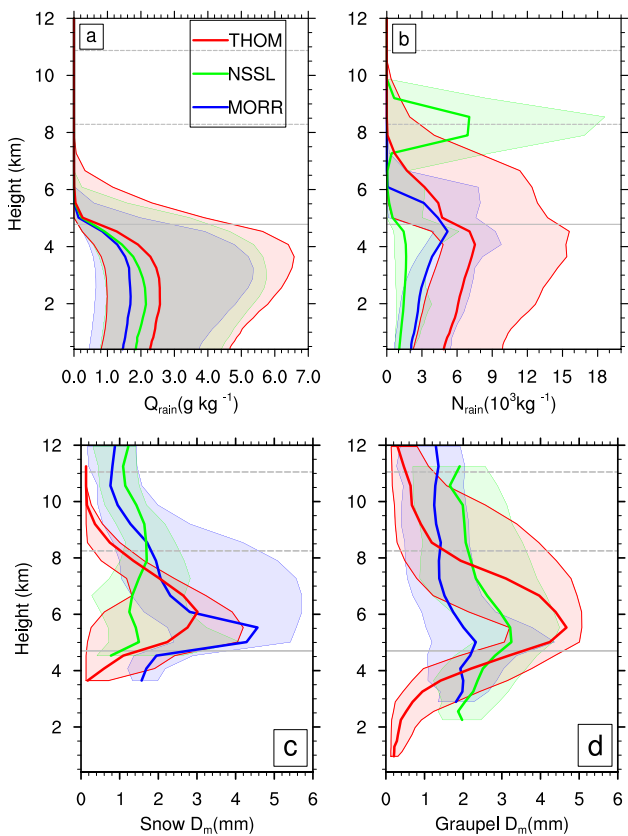


Figure 10. Composite vertical profiles of the mixing ratio (a), and total number concentrations (b) of rain, and the mass-weighted mean diameter of (c) snow, (d) graupel obtained from MORR, NSSL, and THOM experiments. The shaded polygons are the range between 5th and 95th quantiles. The profiles are not shown when the samples size is less than 200 in each layer. The gray lines indicate the level of 0°C, -20°C, and -40°C, respectively.

by ~30–50% (Figure 9a), suggesting that the simulations fail to adequately produce the concentration of medium-sized raindrops in this extreme rainfall case. Besides, the decrease in observed LWC below 3 km altitude not seen in the simulation suggests that the evaporation and advection of the liquid hydrometeor may be underestimated. In addition, the size sorting caused by the increase of large raindrops should also be responsible for the LWC bias. These moisture-related processes are critical in the short-term heavy rainfall event (Huang et al., 2016). Consistent with the accumulated precipitation (Figure 2), the THOM experiment produces the largest median LWC and the rainwater mass content (Q_{rain}), followed by the NSSL and MORR experiments (Figures 9a and 10a).

Although the IWC retrieval method has limited accuracy, the different vertical gradient of the estimated and simulated IWC (rather than absolute values) shed some light on the differences of the ice-phase microphysical processes among simulations. The snow and graupel are considered in the calculation of IWC for each simulation. The peak of observed IWC appears at 5–6.5 km altitude, suggesting that the riming process may be more important than other ice-phase microphysical processes (i.e., aggregation) in the warm-sector extreme rainfall. The three schemes cannot reproduce the ratio of riming processes and other ice-phase processes (Grazioli et al., 2015). It should be noted that the retrieval IWC has large uncertainty, and the above discussion needs to be carefully verified by more accurate observations (i.e., with a balloon-borne hydrometeor videosonde as documented in Sakai et al. (2006)).

Figure 10 shows the mixing ratio and total number concentration of rain, and the mass-weighted mean diameters of snow and graupel. There is an anomalous peak for rain total number concentration in the NSSL experiment at the 8 km height (Figure 10b), but the corresponding mixing ratio is close to 0 g kg⁻¹ (Figure 10a). This indicates the presence of a larger number of very small rain drops at that level with very little mass, which should have little real influence on the precipitation processes. The cloud droplet number concentration is also larger at this level (not shown); apparently the main source of large rain total number concentration is auto-conversion from cloud droplets.

4. Warm-Rain Microphysical Processes

As a typical WR event over inland South China, the “5.7” extreme rainfall event occurred without any obvious synoptic weather system. Sharp decreases in Z_H above the freezing level (Figure 8a) coincident with low echo-top heights indicate that warm-rain processes are significant, where precipitation growth occurs primarily below the freezing level through the collision–coalescence process (Huang et al., 2020). Therefore, we will further analyze the capabilities of the microphysics schemes in simulating the warm-rain processes.

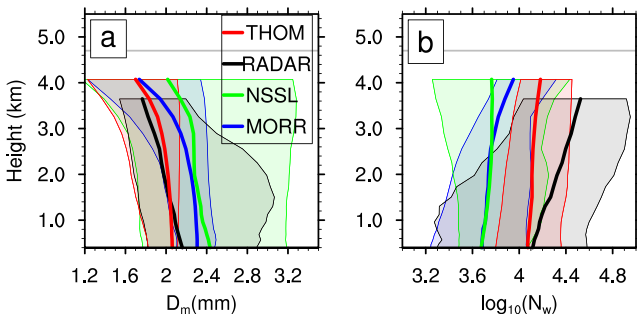


Figure 11. Same as Figure 8, but for (a) D_{mr} (mm) and (b) logarithmic N_{wr} .

The vertical profiles of mass-weighted mean diameter (D_{mr}) and logarithmic normalized intercept ($\log_{10} N_{\text{wr}}$) of raindrops below the melting layer within the convective regions are plotted in Figure 11. All experiments produce larger median raindrop sizes than the observations (Figure 11a), consistent with the median Z_{DR} in Figure 8b. Specifically, the NSSL experiment has the largest bias in median D_{mr} (~0.2 mm), but the best range (the shaded region in Figure 11a). Combined with the vertical profiles of the sizes of snow and graupel particles (Figures 10c and 10d) and the profiles of vertical velocity (Figure 3), the large raindrops near 4 km altitude should come from the melting of large snow and graupel particles. In numerical simulations,

too strong updrafts can lead to overly active ice phase processes, such as riming and aggregation, and therefore unrealistically large graupel/snow particles. These large ice particles fall into the melting layer and melt gradually to become large-sized raindrops. These processes are likely responsible for the raindrop size deviations observed at the bottom of melting layer. In this case, the positive deviation of the raindrop sizes above the 3.5 km altitude can be partly attributed to the excessive simulation of ice particles, especially of large graupel (Wu et al., 2021). Overly active ice phase processes with unrealistically high graupel/snow contents appear to be a common problem for current models with bulk microphysics parameterization (Lang et al., 2011), especially in the warm-type heavy rain from East Asia (Song & Sohn, 2018). It should be noted that the diameter profiles of ice-phase particles extend to different heights due to different sample sizes, especially the graupel (Figure 10d). The distribution of $\log_{10} N_{\text{wr}}$ is opposite of D_{mr} . All three schemes underestimate the number concentration of raindrops in terms of median and range, especially the NSSL and MORR schemes. They have comparable $\log_{10} N_{\text{wr}}$ below 2.6 km, with negative biases exceeding 0.5. In other words, their simulated N_{wr} ($4.5 \times 10^3 \text{ mm}^{-1} \text{ mm}^{-3}$) is only equivalent to one-third of the observations ($1.5 \times 10^4 \text{ mm}^{-1} \text{ mm}^{-3}$). This insufficient rain production in the simulations can contribute to the underestimated surface precipitation. A serious underestimation of raindrop number concentration near the freezing level would reduce the efficiency of the collision–coalescence process (Wang et al., 2020).

The combination of Q_{rain} (Figure 10a) and raindrop total number concentration (N_{rain} , Figure 10b) makes D_{mr} increase toward the ground. From the melting layer to the near surface, the D_{mr} increase from 1.8 to 2.15 mm in the observations, and the $\log_{10} N_{\text{wr}}$ decrease from 4.55 to 4.1 (Figure 11 black lines), implying that the collision–coalescence process is active in the observed convective cells. In comparison, the three experiments exhibit smaller D_{mr} increase rates and $\log_{10} N_{\text{wr}}$ decrease rates, suggesting that the collision–coalescence process is insufficiently active, affecting the growth of raindrops on their way down.

Several studies (Kumjian et al., 2012; Zhang et al., 2006) have demonstrated that it is possible to obtain greater insight into the dominant precipitation microphysical processes by mapping polarimetric radar data onto certain parameter spaces. This study utilizes a parameter space that takes into account the vertical variations of Z_{H} and Z_{DR} , as developed by Kumjian et al. (2012) and referred to as the KR parameter space (after its principal developers). To avoid the interference of terrain and melting layer, the horizontal axis of the KR parameter space is defined by the difference in Z_{H} (δZ_{H} ; dBZ) between the surface (0.4 km) and the bottom of the melting layer (3.4 km). The vertical axis is defined by the difference in Z_{DR} (δZ_{DR} ; dB) over the same vertical layer. The gray text in each quadrant (Figure 12) indicates the dominant warm-rain processes within the KR parameter space, a detailed description of the reasoning behind can be found in Kumjian et al. (2012).

Figure 12 gives the frequency statistics of the KR parameter over the convective regions for the observations and three simulations. Because coalescence is the dominant warm-rain microphysical process during heavy rainfall, it is not surprising that most points lie in the first quadrant (e.g., see the statistical results in Yu et al. (2022)). The proportion of simulated coalescence is, however, lower than that of observations (80.9%). Among the simulations, NSSL produces the lowest proportion of coalescence (61.1%), which can be attributed to the fact that some raindrops at 3.4 km altitude are too large to continually grow via the collision–coalescence process. Meanwhile, the three microphysics schemes also underestimate the intensity of coalescence in terms of the maximum frequency location (red crosses and texts in Figure 12). Compared with the observed δZ_{DR} value of 0.6 dB at the maximum frequency point, the simulated δZ_{DR} values are between 0.0 and 0.1 dB. These results are consistent with the vertical profiles of D_{mr} (Figure 11a) and Z_{DR} (Figure 8b).

It is also notable that 14.6% of observed convective columns are located in quadrant II of the KR parameter space (Figure 12a), corresponding to size sorting and evaporation. While the three simulations underestimate the points in quadrant II with proportions of 12.4%, 4.6% and 12.3%, respectively (Figures 12b–12d). These insufficient evaporation processes may contribute to the underestimated decrease rate of LWC below 3 km (Figure 9a). Besides, the NSSL experiment produces much more breakup of raindrops (i.e., 23.2%) than the observations, suggesting overestimation of the number of large raindrops (Figure 7b). The simulation of supercell (Saleeby et al., 2022) also shows that NSSL and MORR schemes produce more large raindrops than THOM scheme.

The vertical variations of microphysical processes related to rainwater content in the MORR and THOM experiments are then examined (Figure 13). The vertical profiles of average hydrometeor mass content transfer rates over the extreme rainfall regions (red boxes in Figure 1) show that the rainwater conversion from cloud droplets through accretion is dominant below the freezing level, which is consistent with the result of the KR parameter space (Figure 12). Evaporation is the largest sink for rainwater content and is mainly active below the

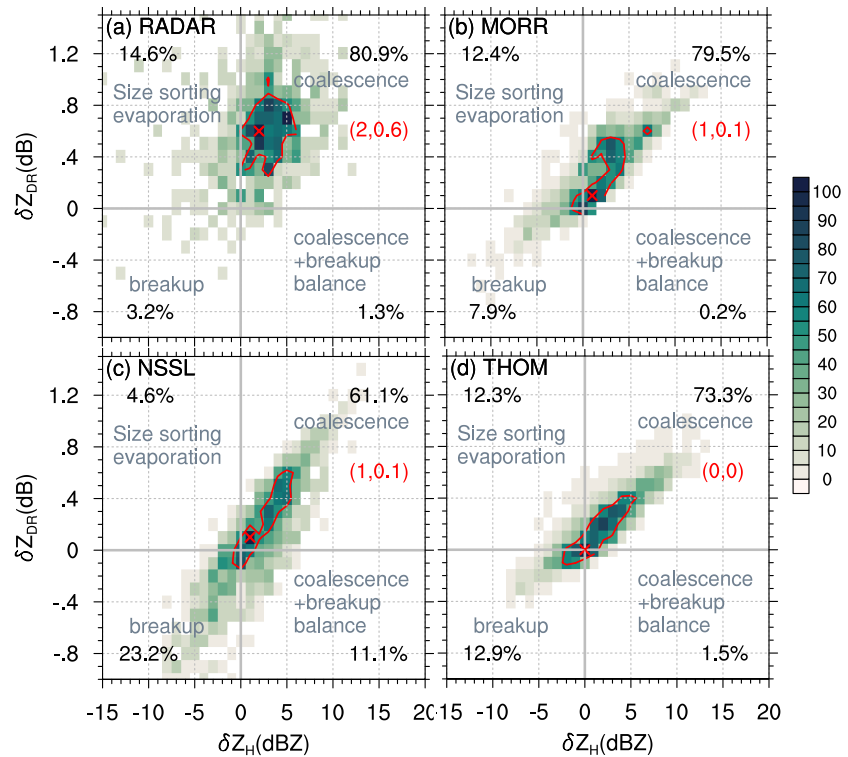


Figure 12. Frequency of occurrences (color shaded) of δZ_H (dBZ) and δZ_{DR} (dB) for the convective area from (a) RADAR, (b) MORR, (c) NSSL, and (d) THOM experiments. The red solid line represents the percentage of 50%. The maximum probability is marked with a cross and its coordinate values are given in red text. The dominant microphysical process and the corresponding probability of occurrence are given in each quadrant.

2.8 km height (i.e., level of 10°C), which confirms the speculation in the quadrant II of the KR parameter space (Figure 12). Graupel melting processes are mostly active within a shallow layer below the freezing level, which is more obvious in the MORR experiment (Figure 13a).

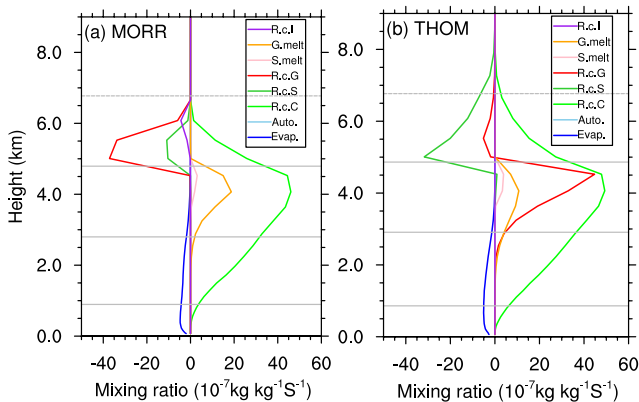


Figure 13. Vertical profiles of average hydrometeor mass transfer rates over the red boxes in Figures 1b and 1d for experiments MORR and THOM from 2300 UTC 6 to 0000 UTC 7 May 2017. The source and sink terms of rain mixing ratio are: Evap., evaporation; Auto., auto-conversion; R.c.C, accretion of cloud droplets by rain; R.c.S, rain collecting snow; R.c.G, rain collecting graupel; S. melt, snow melting; G. melt, graupel melting; R.c.I, rain collecting ice. The gray lines indicate the level of 20, 10, 0, and -10°C from bottom to top.

5. Summary and Conclusions

In this study, the Morrison (MORR), NSSL, and Thompson (THOM) microphysics schemes with their default settings are examined based on the simulations of a local extreme rainfall event over Guangzhou during 6–7 May 2017. To evaluate the capabilities of these microphysics schemes in reproducing the microphysical characteristics of warm sector heavy rainfall, the simulated polarimetric variables and RSD parameters are compared with the Guangzhou polarimetric radar observations and their retrieved variables. In particular, the vertical variations of RSD parameters and the KR parameter space are diagnosed to investigate the dominant warm-rain processes affecting surface precipitation of this event.

Compared to observed precipitation, the three experiments reproduce similar spatial distributions of 15-hr accumulated precipitation. Comparatively speaking, the THOM scheme provides the most amount of precipitation, followed by the NSSL and MORR. While the NSSL scheme reproduces the bimodal distribution of observed precipitation. The vertical profiles of moisture fluxes and the average vertical motion within a small area surrounding the maximum rainfall location indicate deeper convection in the MORR and NSSL experiments than that of THOM experiment.

Overall, the three schemes slightly underestimate (overestimate) the Z_H (Z_{DR}). In terms of the joint frequency distributions of ZH - ZDR and D_{mr} - N_{wr} , the THOM scheme better produces raindrop median size and number concentration, but its mass-weighted mean diameter is cut off at ~ 2.12 mm, resulting from the assumption that no raindrops can be larger than 5 mm in the THOM scheme (Thompson et al., 2008). Compared to observations and the simulation of THOM, both MORR and NSSL experiments present larger raindrop sizes and lower number concentrations, although the NSSL experiment reproduces the shape of observed RSD. In particular, the MORR and NSSL experiments overestimate the occurrence frequencies of large raindrops.

All three experiments have large simulation errors in KDP , with almost ~ 30 – 50% undervaluation below the melting layer. The possible reason is that the microphysics schemes underestimate the number concentration of medium-sized raindrops, resulting in lower liquid water content. For example, the Morrison scheme only produces one-tenth of observed raindrops with sizes of 1.5–2.0 mm, corresponding to the lowest precipitation. The occurrence frequency indicates that these double-moment microphysics schemes fail to reproduce the full observed RSD variability, which should be responsible for the extreme rainfall in this study.

The analysis results suggest that the coalescence is the dominant warm-rain process in all three simulations, with slightly lower proportions than observations. However, from the melting layer toward the ground, the coalescence intensity is significantly weaker than the observations in terms of the increase (decrease) rate of ZDR or D_{mr} (N_{wr}). This may be partly attributed to the assumption on coalescence efficiency in these schemes, which is low for the extreme rainfall. In addition, low initial raindrop concentration and excessively large raindrop size, especially at the height of 3–4 km, may be another important reason. The large raindrops above 3.5 km mainly come from the melting of ice-phase particles (i.e., snow and graupel). Besides, the greater number of large raindrops in the NSSL scheme likely leads to more breakup than observed.

This study documents the behaviors of several double moment microphysics schemes within the WRF model for simulating a warm-sector extreme rainfall event in South China. However, it is important to acknowledge that the conclusions drawn in this study are based on a single case. More case studies should be carried out to determine how general the conclusions of this paper are. In addition, the parameters of the microphysics schemes, including the constant prespecified cloud droplet total number concentration in the MORR and THOM schemes, and the prespecified CCN in the NSSL scheme, are all set to their default values. The performances of these microphysics schemes can be sensitive to the parameter settings, and such sensitivity will require separate in-depth studies. Meanwhile, we want to point out that other errors in the simulation model could compensate errors in microphysics, therefore a better simulation of surface precipitation do not necessarily mean a better microphysics scheme. More systematic evaluations will be needed to draw such conclusions with confidence. The uncertainties and robustness of microphysical processes (e.g., the urban effects, and collection efficiency of between raindrops and other particles) can be more reliably assessed through ensemble simulations with perturbed initial conditions or different physics options. If the key results and conclusions are not sensitive to the initial condition perturbations, then we can trust the conclusions with more confidence. This can be a topic for further study.

Conflict of Interest

The authors declare no conflicts of interest relevant to this study.

Data Availability Statement

The WRF-simulated products, the observed rainfall, and the polarimetric radar products from this study are available at the Harvard Dataverse (Wang, 2023). Figures in this manuscript are produced using the NCAR Command Language (Version 6.6.2) [Software] (2019).

References

- Berry, E. X., & Reinhardt, R. L. (1974). An analysis of cloud drop growth by collection Part II: Single initial distributions. *Journal of the Atmospheric Sciences*, 31(7), 1825–1831. [https://doi.org/10.1175/1520-0469\(1974\)031<1825:aaocdg>2.0.co;2](https://doi.org/10.1175/1520-0469(1974)031<1825:aaocdg>2.0.co;2)
- Braham, R. R., & Squires, P. (1974). Cloud physics—1974. *Bulletin of the American Meteorological Society*, 55(6), 543–586. [https://doi.org/10.1175/1520-0477\(1974\)055<0543:cp>2.0.co;2](https://doi.org/10.1175/1520-0477(1974)055<0543:cp>2.0.co;2)
- Bringi, V. N., Chandrasekar, V., Hubbert, J., Gorgucci, E., Randeu, W. L., & Schoenhuber, M. (2003). Raindrop size distribution in different climatic regimes from disdrometer and dual-polarized Radar analysis. *Journal of the Atmospheric Sciences*, 60(2), 354–365. [https://doi.org/10.1175/1520-0469\(2003\)060<0354:rsdidi>2.0.co;2](https://doi.org/10.1175/1520-0469(2003)060<0354:rsdidi>2.0.co;2)

Acknowledgments

This study is jointly supported by the National Key R&D Program of China (2022YFC3003903), National Natural Science Foundation of China (41730965, 42075083, 42075014), Guangdong Province Natural Sciences fund project (Grant 2022A1515011471).

- Brown, B. R., Bell, M. M., & Frambach, A. J. (2016). Validation of simulated hurricane drop size distributions using polarimetric radar. *Geophysical Research Letters*, 43(2), 910–917. <https://doi.org/10.1002/2015GL067278>
- Carr, N., Kirstetter, P. E., Gourley, J. J., & Hong, Y. (2017). Polarimetric signatures of midlatitude warm-rain precipitation events. *Journal of Applied Meteorology and Climatology*, 56(3), 697–711. <https://doi.org/10.1175/jamc-d-16-0164.1>
- Gao, W., Xue, L., Liu, L., Lu, C., Yun, Y., & Zhou, W. (2021). A study of the fraction of warm rain in a pre-summer rainfall event over South China. *Atmospheric Research*, 262, 105792. <https://doi.org/10.1016/j.atmosres.2021.105792>
- Grazioli, J., Lloyd, G., Panziera, L., Hoyle, C. R., Connolly, P. J., Henneberger, J., & Berne, A. (2015). Polarimetric radar and in situ observations of riming and snowfall microphysics during CLACE 2014. *Atmospheric Chemistry and Physics*, 15(23), 13787–13802. <https://doi.org/10.5194/acp-15-13787-2015>
- Hence, D. A., & Houze, R. A., Jr. (2011). Vertical structure of hurricane eyewalls as seen by the TRMM precipitation radar. *Journal of the Atmospheric Sciences*, 68(8), 1637–1652. <https://doi.org/10.1175/2011JAS3578.1>
- Hong, S.-Y., Noh, Y., & Dudhia, J. (2006). A new vertical diffusion package with an explicit treatment of entrainment processes. *Monthly Weather Review*, 134(9), 2318–2341. <https://doi.org/10.1175/mwr3199.1>
- Huang, L., & Luo, Y. (2017). Evaluation of quantitative precipitation forecasts by TIGGE ensembles for South China during the presummer rainy season. *Journal of Geophysical Research: Atmospheres*, 122(16), 8494–8516. <https://doi.org/10.1002/2017jd026512>
- Huang, S., Li, Z., & Bao, C. (1986). *Heavy rains in the first rainy season of South China (in Chinese)* (p. 230p). Guangdong Science and Technology Press.
- Huang, Y., Cui, X., & Li, X. (2016). A three-dimensional WRF-based precipitation equation and its application in the analysis of roles of surface evaporation in a torrential rainfall event. *Atmospheric Research*, 169, 54–64. <https://doi.org/10.1016/j.atmosres.2015.09.026>
- Huang, Y., Liu, Y., Liu, Y., & Kniviel, J. C. (2019). Budget analyses of a record-breaking rainfall event in the coastal metropolitan city of Guangzhou, China. *Journal of Geophysical Research: Atmospheres*, 124(16), 9391–9406. <https://doi.org/10.1029/2018JD030229>
- Huang, Y., Wang, Y., Xue, L., Wei, X., Zhang, L., & Li, H. (2020). Comparison of three microphysics parameterization schemes in the WRF model for an extreme rainfall event in the coastal metropolitan City of Guangzhou, China. *Atmospheric Research*, 240, 104939. <https://doi.org/10.1016/j.atmosres.2020.104939>
- Johnson, M., Jung, Y., Dawson, D. T. I., & Xue, M. (2016). Comparison of simulated polarimetric signatures in idealized supercell storms using two-moment bulk microphysics schemes in WRF. *Monthly Weather Review*, 144(3), 971–996. <https://doi.org/10.1175/MWR-D-15-0233.1>
- Jung, Y., Zhang, G., & Xue, M. (2008). Assimilation of simulated polarimetric radar data for a convective storm using the ensemble Kalman filter. Part I: Observation operators for reflectivity and polarimetric variables. *Monthly Weather Review*, 136(6), 2228–2245. <https://doi.org/10.1175/2007MWR2083.1>
- Kain, J. S. (2004). The kain–fritsch convective parameterization: An update. *Journal of Applied Meteorology*, 43(1), 170–181. [https://doi.org/10.1175/1520-0450\(2004\)043<0170:tkcpau>2.0.co;2](https://doi.org/10.1175/1520-0450(2004)043<0170:tkcpau>2.0.co;2)
- Kedia, S., Vellore, R. K., Islam, S., & Kaginalkar, A. (2019). A study of Himalayan extreme rainfall events using WRF-Chem. *Meteorology and Atmospheric Physics*, 131(4), 1133–1143. <https://doi.org/10.1007/s00703-018-0626-1>
- Khairoutdinov, M., & Kogan, Y. (2000). A new cloud physics parameterization in a large-eddy simulation model of marine stratocumulus. *Monthly Weather Review*, 128(1), 229–243. [https://doi.org/10.1175/1520-0493\(2000\)128<0229:ancppi>2.0.co;2](https://doi.org/10.1175/1520-0493(2000)128<0229:ancppi>2.0.co;2)
- Kumjian, M. R. (2013). Principles and applications of dual-polarization weather radar. Part I: Description of the polarimetric radar variables. *Journal of Operational Meteorology*, 1(19), 226–242. <https://doi.org/10.15191/jwajom.2013.0119>
- Kumjian, M. R., Ryzhkov, A., Trömel, S., Diederich, M., Mühlbauer, K., & Simmer, C. (2012). Retrievals of warm rain microphysics using X-band polarimetric radar data. *26th Conference on Hydrology*, 406. [Available online at <https://ams.confex.com/ams/492Annual/webprogram/Paper206846.html>]
- Kumjian, M. R., & Ryzhkov, A. V. (2008). Polarimetric signatures in supercell thunderstorms. *Journal of Applied Meteorology and Climatology*, 47(7), 1940–1961. <https://doi.org/10.1175/2007JAMC1874.1>
- Lang, S. E., Tao, W.-K., Zeng, X., & Li, Y. (2011). Reducing the biases in simulated radar reflectivities from a bulk microphysics scheme: Tropical convective systems. *Journal of the Atmospheric Sciences*, 68(10), 2306–2320. <https://doi.org/10.1175/JAS-D-10-05000.1>
- Liu, X., Luo, Y., Guan, Z., & Zhang, D.-L. (2018). An extreme rainfall event in coastal South China during SCMRX-2014: Formation and roles of rainband and echo trainings. *Journal of Geophysical Research: Atmospheres*, 123(17), 9256–9278. <https://doi.org/10.1029/2018JD028418>
- Lou, X., Hu, Z., Shi, Y., Wang, P., & Zhou, X. (2003). Numerical simulations of a heavy rainfall case in South China. *Advances in Atmospheric Sciences*, 20(1), 128–138. <https://doi.org/10.1007/BF03342057>
- Lu, C., Zhu, L., Liu, Y., Mei, F., Fast, J. D., Pekour, M. S., et al. (2023). Observational study of relationships between entrainment rate, homogeneity of mixing, and cloud droplet relative dispersion. *Atmospheric Research*, 293, 106900. <https://doi.org/10.1016/j.atmosres.2023.106900>
- Luo, Y., Xia, R., & Chan, J. C. L. (2020). Characteristics, physical mechanisms, and prediction of pre-summer rainfall over South China: Research progress during 2008–2019. *Journal of the Meteorological Society of Japan. Series II*, 98(1), 19–42. <https://doi.org/10.2151/jmsj.2020-002>
- Luo, Y., Zhang, R., Wan, Q., Wang, B., Wong, W. K., Hu, Z., et al. (2017). The southern China monsoon rainfall experiment (SCMRX). *Bulletin of the American Meteorological Society*, 98(5), 999–1013. <https://doi.org/10.1175/BAMS-D-15-00235.1>
- Mansell, E. R., Ziegler, C. L., & Bruning, E. C. (2010). Simulated electrification of a small thunderstorm with two-moment bulk microphysics. *Journal of the Atmospheric Sciences*, 67(1), 171–194. <https://doi.org/10.1175/2009JAS2965.1>
- Malaver, E. J., Taubman, S. J., Brown, P. D., Iacono, M. J., & Clough, S. A. (1997). Radiative transfer for inhomogeneous atmospheres: RRTM, a validated correlated-k model for the longwave. *Journal of Geophysical Research*, 102(D14), 16663–16682. <https://doi.org/10.1029/97JD00237>
- Morrison, H., Thompson, G., & Tatarskii, V. (2009). Impact of cloud microphysics on the development of trailing stratiform precipitation in a simulated squall line: Comparison of one- and two-moment schemes. *Monthly Weather Review*, 137(3), 991–1007. <https://doi.org/10.1175/2008mwr2556.1>
- NCAR Command Language. (2019). NCAR Command Language (version 6.6.2), [software] (p. 753). UCAR/NCAR/CISL/TDD. <https://doi.org/10.5065/D6WD3XH5>
- Niu, G.-Y., Yang, Z.-L., Mitchell, K. E., Chen, F., Ek, M. B., Barlage, M., et al. (2011). The community Noah land surface model with multiparameterization options (Noah-MP): 1. Model description and evaluation with local-scale measurements. *Journal of Geophysical Research*, 116(D12), D12109. <https://doi.org/10.1029/2010JD015139>
- Putnam, B. J., Xue, M., Jung, Y., Snook, N., & Zhang, G. (2014). The analysis and prediction of microphysical states and polarimetric radar variables in a mesoscale convective system using double-moment microphysics, multinet radar data, and the ensemble Kalman filter. *Monthly Weather Review*, 142(1), 141–162. <https://doi.org/10.1175/mwr-d-13-00042.1>
- Putnam, B. J., Xue, M., Jung, Y., Snook, N. A., & Zhang, G. (2017). Ensemble probabilistic prediction of a mesoscale convective system and associated polarimetric radar variables using single-moment and double-moment microphysics schemes and EnKF radar data assimilation. *Monthly Weather Review*, 145(6), 2257–2279. <https://doi.org/10.1175/MWR-D-16-0162.1>

- Putnam, B. J., Xue, M., Jung, Y., Zhang, G., & Kong, F. (2017). Simulation of polarimetric radar variables from 2013 CAPS spring experiment storm scale ensemble forecasts and evaluation of microphysics schemes. *Monthly Weather Review*, *145*(1), 49–73. <https://doi.org/10.1175/MWR-D-15-0415.1>
- Ryzhkov, A., Bukovcic, P., Murphy, A., Zhang, P., & McFarquhar, G. (2018). Ice microphysical retrievals using polarimetric radar data. *10th European Conference on Radar in Meteorology and Hydrology*, 40, 1–6.
- Sakai, T., Orikasa, N., Nagai, T., Murakami, M., Kusunoki, K., Mori, K., et al. (2006). Optical and microphysical properties of upper clouds measured with the Raman lidar and hydrometeor videonode: A case study on 29 March 2004 over Tsukuba, Japan. *Journal of the Atmospheric Sciences*, *63*(8), 2156–2166. <https://doi.org/10.1175/JAS3736.1>
- Saleeby, S. M., Dolan, B., Bukowski, J., Van Valkenburg, K., Van den Heever, S. C., & Rutledge, S. A. (2022). Assessing raindrop breakup parameterizations using disdrometer observations. *Journal of the Atmospheric Sciences*, *79*(11), 2949–2963. <https://doi.org/10.1175/JAS-D-21-0335.1>
- Seaman, N. L., Stauffer, D. R., & Lario-Gibbs, A. M. (1995). A multiscale four-dimensional data assimilation system applied in the san joaquin valley during SARMAP. Part I: Modeling design and basic performance characteristics. *Journal of Applied Meteorology and Climatology*, *34*(8), 1739–1761. [https://doi.org/10.1175/1520-0450\(1995\)034<1739:amfdda>2.0.co;2](https://doi.org/10.1175/1520-0450(1995)034<1739:amfdda>2.0.co;2)
- Song, H.-J., & Sohn, B.-J. (2018). An evaluation of WRF microphysics schemes for simulating the warm-type heavy rain over the Korean Peninsula. *Asia-Pacific Journal of Atmospheric Sciences*, *54*(2), 1–236. <https://doi.org/10.1007/s13143-018-0006-2>
- Tao, W.-K., Shie, C.-L., Simpson, J., Braun, S., Johnson, R. H., & Ciesielski, P. E. (2003). Convective systems over the South China Sea: Cloud-resolving model simulations. *Journal of the Atmospheric Sciences*, *60*(24), 2929–2956. [https://doi.org/10.1175/1520-0469\(2003\)060<2929:csotsc>2.0.co;2](https://doi.org/10.1175/1520-0469(2003)060<2929:csotsc>2.0.co;2)
- Thompson, G., Field, P. R., Rasmussen, R. M., & Hall, W. D. (2008). Explicit forecasts of winter precipitation using an improved bulk microphysics scheme. Part II: Implementation of a new snow parameterization. *Monthly Weather Review*, *136*(12), 5095–5115. <https://doi.org/10.1175/2008MWR2387.1>
- Twomey, S. (1959). The nuclei of natural cloud formation part II: The supersaturation in natural clouds and the variation of cloud droplet concentration. *Geofisica pura e applicata*, *43*(1), 243–249. <https://doi.org/10.1007/BF01993560>
- Wang, H. (2023). Replication data for JGR: Atmospheres [dataset]. Harvard Dataverse. <https://doi.org/10.7910/DVN/NFXPPN>
- Wang, H., Kong, F., Jung, Y., Wu, N., & Yin, J. (2018). Quality control of S-band polarimetric radar measurements for data assimilation. *Journal of Applied Meteorology and Science*, *29*(5), 546–558. (in Chinese with an English abstract). <https://doi.org/10.11898/1001-7313.20180504>
- Wang, H., Kong, F., Wu, N., Lan, H., & Yin, J. (2019). An investigation into microphysical structure of a squall line in South China observed with a polarimetric radar and a disdrometer. *Atmospheric Research*, *226*, 171–180. <https://doi.org/10.1016/j.atmosres.2019.04.009>
- Wang, H., Wan, Q., Yin, J., & Ding, W. (2016). Application of the dual-polarization radar data in numerical model: Construction of simulator. *Acta Meteorologica Sinica*, *74*(02), 229–243. (in Chinese with an English abstract). <https://doi.org/10.11676/qxxb2016.017>
- Wang, H., Yin, J., Wu, N., & Ding, W. (2023). Microphysical structures of an extreme rainfall event over the coastal metropolitan city of Guangzhou, China: Observation analysis with polarimetric radar. *Asia-Pacific Journal of Atmospheric Sciences*, *59*(1), 3–16. <https://doi.org/10.1007/s13143-022-00289-y>
- Wang, M., Zhao, K., Pan, Y., & Xue, M. (2020). Evaluation of simulated drop size distributions and microphysical processes using polarimetric radar observations for landfalling typhoon Matmo (2014). *Journal of Geophysical Research: Atmospheres*, *125*(6), e2019JD031527. <https://doi.org/10.1029/2019JD031527>
- Wu, D., Zhang, F., Chen, X., Ryzhkov, A., Zhao, K., Kumjian, M. R., et al. (2021). Evaluation of microphysics schemes in tropical cyclones using polarimetric radar observations: Convective precipitation in an outer rainband. *Monthly Weather Review*, *149*(4), 1055–1068. <https://doi.org/10.1175/mwr-d-19-0378.1>
- Wu, Z., Cai, J., Lin, L., Hu, S., Zhang, H., & Wei, K. (2018). Analysis of mesoscale system and predictability of the torrential rain process in Guangzhou on 7 May 2017. *Meteorological Monthly*, *44*(4), 485–499. (in Chinese with an English abstract). <https://doi.org/10.7519/j.issn.1000-0526.2018.04.002>
- Xiao, H., Liu, X., Li, H., Yue, Q., Feng, L., & Qu, J. (2023). Extent of aerosol effect on the precipitation of squall lines: A case study in South China. *Atmospheric Research*, *292*, 106886. <https://doi.org/10.1016/j.atmosres.2023.106886>
- Xu, J., Bi, B., Chen, Y., Chen, T., Gong, Y., & Li, J. (2018). Mesoscale characteristics and mechanism analysis of the unexpected local torrential rain in Guangzhou on 7 May 2017. *Acta Meteorologica Sinica*, *76*(4), 511–524. (in Chinese with an English abstract). <https://doi.org/10.11676/qxxb2018.016>
- Xu, X., Lu, C., Liu, Y., Gao, W., Wang, Y., Cheng, Y., et al. (2020). Effects of cloud liquid-phase microphysical processes in mixed-phase cumuli over the Tibetan Plateau. *Journal of Geophysical Research: Atmospheres*, *125*(19), e2020JD033371. <https://doi.org/10.1029/2020JD033371>
- Yang, L., Smith, J., Liu, M., & Baeck, M. L. (2019). Extreme rainfall from hurricane Harvey (2017): Empirical intercomparisons of WRF simulations and polarimetric radar fields. *Atmospheric Research*, *223*, 114–131. <https://doi.org/10.1016/j.atmosres.2019.03.004>
- Yin, J., Zhang, D.-L., Luo, Y., & Ma, R. (2020). On the extreme rainfall event of 7 may 2017 over the coastal city of Guangzhou. Part I: Impacts of urbanization and orography. *Monthly Weather Review*, *148*(3), 955–979. <https://doi.org/10.1175/MWR-D-19-0212.1>
- You, C.-R., Chung, K.-S., & Tsai, C.-C. (2020). Evaluating the performance of a convection-permitting model by using dual-polarimetric radar parameters: Case study of SOWMEX IOP8. *Remote Sensing*, *12*(18), 3004. <https://doi.org/10.3390/rs12183004>
- Yu, S., Luo, Y., Wu, C., Zheng, D., Liu, X., & Xu, W. (2022). Convective and microphysical characteristics of extreme precipitation revealed by multisource observations over the Pearl River Delta at monsoon coast. *Geophysical Research Letters*, *49*(2), e2021GL097043. <https://doi.org/10.1029/2021GL097043>
- Zhang, D., & Anthes, R. A. (1982). A high-resolution model of the planetary boundary layer—Sensitivity tests and comparisons with SESAME-79 data. *Journal of Applied Meteorology and Climatology*, *21*(11), 1594–1609. [https://doi.org/10.1175/1520-0450\(1982\)021<1594:ahrmot>2.0.co;2](https://doi.org/10.1175/1520-0450(1982)021<1594:ahrmot>2.0.co;2)
- Zhang, G., Mahale, V. N., Putnam, B. J., Qi, Y., Cao, Q., Byrd, A. D., et al. (2019). Current status and future challenges of weather radar polarimetry: Bridging the gap between radar meteorology/hydrology/engineering and numerical weather prediction. *Advances in Atmospheric Sciences*, *36*(6), 571–588. <https://doi.org/10.1007/s00376-019-8172-4>
- Zhang, G., Sun, J., & Brandes, E. A. (2006). Improving parameterization of rain microphysics with disdrometer and radar observations. *Journal of the Atmospheric Sciences*, *63*(4), 1273–1290. <https://doi.org/10.1175/jas3680.1>
- Zhao, K., Huang, H., Wang, M., Lee, W.-C., Chen, G., Wen, L., et al. (2019). Recent progress in dual-polarization radar research and applications in China. *Advances in Atmospheric Sciences*, *36*(9), 961–974. <https://doi.org/10.1007/s00376-019-9057-2>
- Ziegler, C. L. (1985). Retrieval of thermal and microphysical variables in observed convective storms. Part I: Model development and preliminary testing. *Journal of the Atmospheric Sciences*, *42*(14), 1487–1509. [https://doi.org/10.1175/1520-0469\(1985\)042<1487:ROTAMV>2.0.CO;2](https://doi.org/10.1175/1520-0469(1985)042<1487:ROTAMV>2.0.CO;2)